Advanced Monte Carlo Simulations of the Adsorption of Chiral Alcohols in a Homochiral Metal-Organic Framework

Zhiwei Qiao
School of Chemistry and Chemical Engineering, Guangdong Provincial Key Lab for Green Chemical Product Technology, South China University of Technology, Guangzhou 510640, China

Dept. of Chemical and Biological Engineering, Northwestern University, 2145 Sheridan Road, Evanston, IL 60208

Ariana Torres-Knoop and David Dubbeldam
Van 't Hoff Institute for Molecular Sciences, University of Amsterdam, Science Park 904, 1098XH Amsterdam, The Netherlands

David Fairen-Jimenez
Dept. of Chemical and Biological Engineering, Northwestern University, 2145 Sheridan Road, Evanston, IL 60208

Dept. of Chemical Engineering and Biotechnology, University of Cambridge, Pembroke Street, Cambridge CB2 3RA, U.K

Jian Zhou
School of Chemistry and Chemical Engineering, Guangdong Provincial Key Lab for Green Chemical Product Technology, South China University of Technology, Guangzhou 510640, China

Randall Q. Snurr
Dept. of Chemical and Biological Engineering, Northwestern University, 2145 Sheridan Road, Evanston, IL 60208

DOI 10.1002/aic.14415
Published online March 1, 2014 in Wiley Online Library (wileyonlinelibrary.com)

Grand canonical Monte Carlo (GCMC) simulations with configurational biasing were used to study the enantioselective adsorption of four alkanols in a homochiral metal-organic framework, known as hybrid organic-inorganic zeolite analogue HOIZA-1. Conventional GCMC simulations are not able to converge satisfactorily for this system due to the tight fit of the chiral alcohols in the narrow pores. However, parallel tempering and parallel mole-fraction GCMC simulations overcome this problem. The simulations show that the enantioselective adsorption of the different (R,S)-alkanols is due to the specific geometry of the chiral molecules relative to the pore size and shape. © 2014 American Institute of Chemical Engineers *AIChE J*, 60: 2324–2334, 2014
Keywords: molecular simulation, metal-organic framework, chiral separation, butanol, enantioselectivity

Introduction

The ubiquitous presence of chirality in biology makes the production of pure enantiomers a fundamental segment of the pharmaceutical, agricultural, and food industries. Particularly for pharmaceuticals, there is now great emphasis on the development of new techniques for asymmetric synthesis and enantiomeric separation. While some chiral molecules are conducive to human health, their enantiomers can have different pharmacologic and toxicologic impacts and can be harmful or toxic in some cases. Asymmetric synthesis is an elegant solution when it is available, but sometime it is easier and more economical to synthesize molecules in racemic mixtures and then separate the enantiomers.[1,2]

A number of methods are currently practiced for chiral separations, including crystallization, kinetic resolution, membrane separations, and chromatography. In particular, chiral chromatography is one of the most important tools for producing single enantiomer compounds.[3–6] Chiral chromatography is based on the free energy differences of the diastereomeric complexes formed between the enantiomers and the chiral stationary phase (CSP).[7] One difficulty is that the enantioselectivities of homologous chiral compounds with similar structures may be hard to predict when separated on the same CSP.[8–11] A small structural change in a chiral compound often leads to no, or even opposite, enantioselectivity, which makes the selection of CSPs difficult. This problem has resulted in a long-standing interest in the development of new materials for this application, as well as broad research efforts focusing on the origin of selective chiral

Additional Supporting Information may be found in the online version of this article.

Correspondence concerning this article should be addressed to R.Q. Snurr at snurr@northwestern.edu or J. Zhou at jianzhou@scut.edu.cn.

adsorption.[1,4] Nevertheless, due to lack of an efficient experimental way to probe chiral separation mechanisms at the molecular level, many conclusions are based on hypotheses and speculations.

Over the past decade, homochiral metal-organic frameworks (HMOFs) have attracted a great deal of attention for selective separation of enantiomers.[12–23] HMOFs are chiral nanoporous crystalline materials composed of metal ions or metal clusters linked by organic ligands. An important advantage of chiral MOFs over traditional CSPs is that MOFs are microporous materials, giving them much larger capacities. Larger capacity may lead to a reduction in solvent usage and higher separation rates. The crystallinity of MOFs also offers significant advantages for tailoring the properties such as the pore-size distribution (PSD) in a controlled way, as well as for accomplishing accurate computational modeling. Although chiral separation on HMOFs has been reported experimentally,[24,25] the separation mechanisms are still not well understood.

Molecular simulation is a powerful tool for predicting adsorption properties and improving our understanding of adsorption behavior at the atomic level and is well suited for studying chiral separation mechanisms.[26] In particular, grand canonical Monte Carlo (GCMC) simulations can be used to predict adsorption isotherms[27–31] and can be adapted to handle chiral compounds. For example, Moghadam and Düren examined the nature of enantioselectivity in the homochiral MOF Ni_2(L-asp)$_2$(bipy) for a number of chiral diols.[32] They found that the level of enantioselectivity was highly dependent on the molecular chain length and the position of the hydroxyl groups. Cann and coworkers simulated chiral separation on several stationary phases for liquid chromatography using molecular dynamics simulations and found that an increase of the alcohol concentration changed the preferred orientations of the selectors.[33–35] In addition, Bao et al. showed that different regions of an HMOF channel may present opposite enantioselectivities[36] and that multiple chiral selectors packed in HMOF structures may work synergistically to improve the chiral separation effect.[37] Bao et al. also studied a model group of homologous alkan-2-ols for chiral separation in HMOFs.[38]

Simulating chiral adsorption can be difficult because most chiral molecules of interest are liquids at ambient conditions. Under liquid-phase conditions, the adsorbent pores are full of adsorbate molecules and the insertion and deletion efficiencies in GCMC simulations are very low, which can affect the reliability and accuracy of the simulations. To increase the efficiency of Monte Carlo simulations and the number of successful insertions and deletions at high density, the configurational-bias Monte Carlo (CBMC) method was developed.[39,40] In CBMC, the insertions are biased toward energetically favorable configurations. Rigid molecules can be biased using different orientations; flexible chain molecules are grown atom-by-atom, biasing the growth to avoid overlap with the pore walls and other molecules. However, as shown here, for some systems the CBMC method is still not efficient enough to produce reliable results.

In this work, we have implemented parallel tempering Monte Carlo (PT MC)[41–46] and parallel mole-fraction Monte Carlo (PMF MC)[47,48] to improve the acceptance of the GCMC simulation moves. In PT MC and PMF MC, replicas of the original system are simulated in parallel at increasing temperatures or different mole fractions, respectively. At regular intervals, replicas at adjacent temperatures or mole fractions are swapped. The system of interest is usually at ambient conditions where entropic barriers and meta-stable states hamper the sampling efficiency. However, at high temperatures, these free energy barriers are reduced.[49] A PT chain is constructed by connecting the low temperature system of interest to the high temperature system in a chain of systems with increasing temperatures. A Monte Carlo "swapping move" exchanges the molecular configurations between neighboring systems that are fixed at different temperatures. The temperature differences are chosen to achieve good acceptance of the swap moves. PT allows the study of the low temperature system of interest with the sampling efficiency of high temperature systems. PMF MC uses a chain of systems with varying mole fraction (instead of the temperature): from 0 to 1 for component A and 1 to 0 for component B.

The problem of interest in this work is the separation of four chiral alkanols using a microporous chiral MOF reported by Xiong et al.[50] They refer to it as a hybrid organic-inorganic zeolite analogue (HOIZA), and we will denote it here as HOIZA-1. HOIZA-1 is synthesized from Cd and the enantiopure building block 6-methoxyl-(8S,9R)-cinchonan-9-ol-3-carboxylic acid (HQA). The resulting material has the formula Cd(QA)$_2$ and possesses a homochiral 3D channel, as shown in Supporting Information Figure S1a. We first describe our model and simulation methodology focusing on the PT and PMF methods. Then, we present the results for the enthalpy of adsorption at infinite dilution to study the interactions of a single molecule with the framework. Next, we compare the separation of (R,S)-2-butanol using conventional GCMC, PT GCMC, and PMF GCMC and show that PT and PMF GCMC are more efficient than conventional GCMC. Finally, we extend our study to the separation of four chiral alkanol molecules and analyze the adsorption geometries to better understand the observed selectivities.

Computational Methods

Model and GCMC simulations

The HOIZA-1 crystal structure (Supporting Information Figure S1a) was modeled as a rigid framework using the crystallographic structure from the literature.[50] The PSD was calculated geometrically from the crystal structure using the method of Gelb and Gubbins.[51] It shows the existence of one main cavity with a pore diameter around 4.5 Å (Supporting Information Figure S1b). The pores are just large enough to accommodate alkanols, and it is, therefore, expected that the molecules will have a strong interaction with the framework.

We used the standard 12-6 Lennard-Jones (LJ) potential to model the dispersive and repulsive interatomic interactions, with a cutoff of 11 Å. The LJ parameters for HOIZA-1 were taken from the universal force field,[52] while the Optimized Potentials for Liquid Simulations (OPLS) all-atom (AA) force field[53,54] was used to model the flexible alkanol molecules. Supporting Information Tables S1 and S2 list all force field parameters. The alkanol structures are displayed in Supporting Information Figure S2. The Lorentz-Berthelot combining rules were used to calculate fluid-framework cross interaction parameters. The partial charges on the alkanol atoms were taken from the OPLS-AA force field,[53,54] while the charges of the HOIZA-1 atoms were estimated using the

Charges from Electrostatic Potentials using a Grid method (CHELPG)[55] and density functional theory calculations with the B3LYP functional[56,57] and the LANL2DZ basis set on a representative portion of the MOF. These HOIZA-1 partial charges are presented in Supporting Information Figure S3. We calculated the adsorbate–adsorbent and adsorbate–adsorbate electrostatic interactions using the Ewald summation technique.[58]

GCMC simulations were performed under liquid-phase conditions at 1–100 bar and a temperature of 300 K. The input fugacities were calculated from the temperature and pressure using the Peng–Robinson equation of state. During the simulations, configurational-biased insertion, deletion, regrowth, and partial regrowth moves, along with random translation and rotation moves of the adsorbate molecules, were used to achieve equilibration. All mixture simulations included identity change moves (i.e., attempts were made to change a randomly chosen R molecule from R to S or vice versa). Configurational-biased moves for branched molecules used the scheme of Vlugt et al.[40] Each simulation point consisted of 6×10^5 cycles, where a cycle consists of N Monte Carlo moves and N is the number of molecules in the system (which fluctuates in GCMC). The first 1×10^5 cycles were used for initialization and the last 5×10^5 cycles were used for accumulating averages. Each simulation point was run independently. Error bars were calculated by dividing the simulation into five sequential "blocks" after the system reached equilibrium. The standard deviation of the block averages was used as an estimate of the error bar.

Enthalpy of adsorption simulations

The enthalpies of adsorption at infinite dilution can be obtained from simulations of a single guest molecule in the framework using

$$\Delta H = \langle \mathcal{V}_{\mathrm{gh}} \rangle - \langle \mathcal{V}_{\mathrm{h}} \rangle - \langle \mathcal{V}_{\mathrm{g}} \rangle - RT \tag{1}$$

where $\mathcal{V}_{\mathrm{gh}}$ is the potential energy of the guest molecule inside the host framework, $\mathcal{V}_{\mathrm{h}}$ is the energy of the empty host framework (here, zero, because the framework is kept rigid), and $\mathcal{V}_{\mathrm{g}}$ is the energy of the isolated guest molecule (contributions from the intramolecular interactions such as bond stretching, bond bending, torsion, and intramolecular van der Waals and Coulombic interactions). MC moves included translation, rotation, reinsertion at a random position, and partial regrowth where random parts of the molecule were regrown. Conventional NVT MC enthalpy simulations used 2.5×10^5 production cycles for both the simulation with a molecule inside the host system and for the isolated molecule. PT NVT simulations used 5×10^4 production cycles for the simulations inside the host system.

PT GCMC and PMF GCMC simulations

For the PT simulations, we followed the algorithm described by Geyer and Thompson.[59] Additional replicas of the system were simulated at higher temperatures, with occasional swaps of configurations between neighboring replicas. The method is designed to overcome the energy barriers between configurations and efficiently sample different configurations and loadings. Each replica was simulated at a different temperature, but the fugacities were kept fixed for all replicas. The partition function for the entire system of replicas can then be written as

$$\Xi_{\text{entire system}} = \prod_{i=1}^{M} \Xi_i(f_1, f_2, V, T_i) \tag{2}$$

where f_1 and f_2 are the fugacities of components 1 and 2; M is the number of replicas; T_i is the absolute temperature of replica i; V is the volume; and Ξ_i is the grand canonical partition function for a single replica and is given by

$$\Xi(f_1, f_2, V, T_i) = \sum_{N_1=0}^{\infty} \sum_{N_2=0}^{\infty} \frac{(\beta f_1 V)^{N_1} (\beta f_2 V)^{N_2}}{N_1! N_2!} \int_V \cdots \int_V e^{-\beta \mathcal{V}} dr^{N_1} dr^{N_2} \tag{3}$$

In the above equation, $\beta = 1/k_{\mathrm{B}}T$, where k_{B} is Boltzmann's constant; N_1 and N_2 are the number of molecules of components 1 and 2; $\mathcal{V}$ is the potential energy of the system; and r represents all the coordinates of a molecule. Note that here the components 1 and 2 are the different enantiomers R and S. During the simulation, configurations from replicas having adjacent temperatures are exchanged at regular intervals. The acceptance rule for exchange between two replicas at temperatures T_a and T_b is given by[46]

$$P_{\mathrm{acc}} = min\left\{1, exp\left[(\beta_b - \beta_a)(\mathcal{V}_b - \mathcal{V}_a)\right]\left(\frac{T_b}{T_a}\right)^{(N_b - N_a)}\right\} \tag{4}$$

(Note that Eq. 3 in Ref. [46] contains a typographical error; a and b in the term (T_b/T_a) were mislabeled; all simulations were, however, performed with the correct acceptance rule.)

We chose the temperatures by simulating 10 different temperatures and comparing their energy histograms $P(E)$. The optimal temperature spacing occurs when the energy histograms of two neighboring temperatures partly overlap. If the temperature gap is too small, then the configurations at different temperatures will be very similar. This will result in an increased computational cost with no gain in simulation efficiency. Conversely, if the temperature gap is too large, there will be no overlap in the histograms, and consequently the probability of successful swaps between configurations at different temperatures will be very low. Based on preliminary calculations, the parallel tempering simulations were performed at 300, 320, 340, 370, 400, 440, 480, 540, 600, and 700 K. Replica swaps were randomly attempted on average once per cycle. In a MC cycle, on average one MC move has been performed per molecule. In addition to the replica swap moves, the PT GCMC simulations included the same particle moves as regular GCMC, namely translation and rotation moves along with configurational-biased insertion, deletion, regrowth, partial regrowth, and (for mixtures) identity change moves. The number of trial positions for configurational biasing was 10, and the insertion of the first atom was biased using 10 random positions in the simulation cell. Both the initialization and production phases were 1×10^5 cycles.

Figure 1a shows the energy histograms obtained from the PT GCMC simulation of (R,S)-2-butanol in HOIZA-1. Note the overlap between the distributions of neighboring temperatures: the larger the overlap of the histograms, the higher the configuration swap probability. Given the overlap of curves in Figure 1 and the observed acceptance ratio of parallel tempering swap moves (ca. 10% between the two lowest temperatures), the selected temperature range is sufficient to produce a high probability of swaps between neighboring replicas.

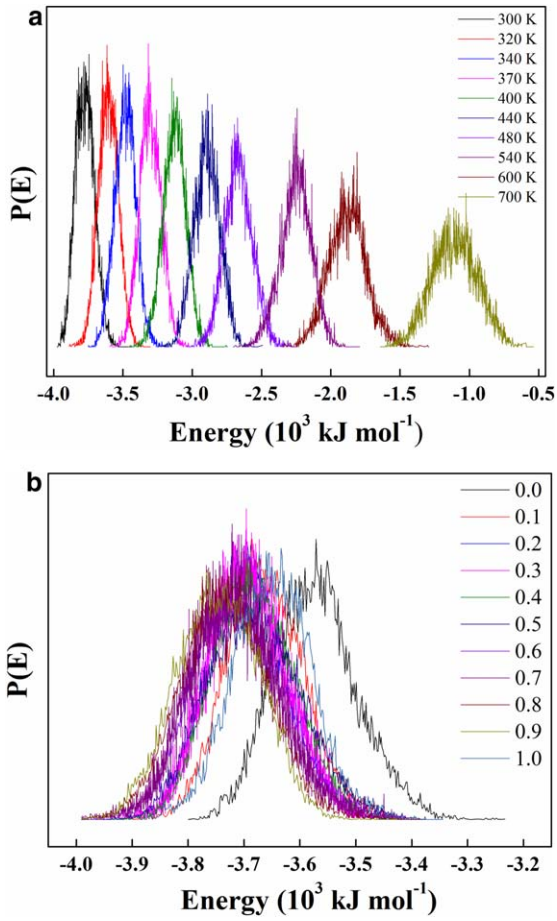

Figure 1. Energy histograms for (R,S)-2-butanol at 1 bar: (a) 10 systems from 300 to 700 K and (b) 11 systems at 300 K with different mole fractions varying from 0 to 1.

[Color figure can be viewed in the online issue, which is available at wileyonlinelibrary.com.]

For parallel mole fraction simulations, the extended variable is not temperature but the mole fractions. This method applies to grand-canonical systems that have the same temperature and total fugacity ($\sum f_\alpha$) but differ in mole fractions (and hence fugacities, f_α, of individual species α). The general distribution of an adsorbent that is in contact with a multicomponent gas follows from the grand canonical ensemble

$$\rho_\xi \propto \frac{e^{-[\beta(\mathcal{V}(\mathbf{r})-\mathbf{n}\cdot\mu)]}}{\Pi_\alpha \Lambda_\alpha^{3n_\alpha}} = e^{-\beta\mathcal{V}(r)}(\beta P)^n \prod_\alpha \xi_\alpha^{n_\alpha} \tag{5}$$

where $\mathcal{V}$ is the total energy of configuration point $\mathbf{r}$ describing all atomic positions; $\boldsymbol{n}$ is the number vector which denotes the number of molecules for each species α such that $\sum_\alpha n_\alpha = n$ is the total number of adsorbed molecules; ξ denotes the mole fraction of these species in the external fluid phase such that $\sum_\alpha \xi_\alpha = 1$; μ denotes the corresponding chemical potential. The probability of a system with gas mole fractions ξ and ξ' in states $\{\boldsymbol{n},\boldsymbol{r}\}$ and $\{\boldsymbol{n}',\boldsymbol{r}'\}$ is simply given by the product of the individual ensemble probabilities. The acceptance rule of a MC move that changes all particle positions from one system to the other is given by[47,48]

$$P_{\text{acc}}(n,r \leftrightarrow n',r') = \min\left[1, \frac{\rho_\xi(n',r')\rho_{\xi'}(n,r)}{\rho_\xi(n,r)\rho_{\xi'}(n',r')}\right] = \min\left[1, \frac{\prod_\alpha \xi_\alpha^{n'_\alpha}\prod_\beta \xi'^{n_\beta}_\beta}{\prod_\alpha \xi_\alpha^{n_\alpha}\prod_\beta \xi'^{n'\beta}_\beta}\right] \tag{6}$$

where the Einstein summation convention has been used.

A chain of systems is constructed from pure R to pure S with a smooth variation in the ratio of R to S. Since both extremes are usually well defined (i.e., they correspond to the pure components) and the energy difference between neighboring systems is now much smaller (see Figure 1b), we might expect improved sampling compared to GCMC. The PMF simulations used replicas at a fixed temperature of 300 K but with different mole fractions of the R enantiomer going from 0 to 1, in steps of 0.1.

Results and Discussion

Infinite dilution enthalpies of adsorption

The computed enthalpies of adsorption in Figure 2 provide information about the interaction of a single molecule with the HOIZA-1 framework. The MOF has a preference for R-2-butanol over S-2-butanol (about 5 kJ/mol) but more strongly adsorbs S-2-pentanol over R-2-pentanol (about 8 kJ/mol energy difference). For 2-methyl-1-butanol and 3-methyl-2-butanol, the S enantiomers are preferred over the R enantiomers by about 10 and 1 kJ/mol, respectively, at room temperature. As noted above, chiral compounds in a homologous series often show inconsistent enantioselectivities when separated on the same CSP,[38] and the results here also display this behavior. The reasons for this behavior are elucidated below.

The conventional Monte Carlo results in Figure 2 are scattered with rather large error bars. These single molecule simulations are fast, but even after long simulation times the results are not converged (the conventional MC simulations were run 5–10 times longer than the PT simulations), especially at low temperatures. The parallel tempering results show a dramatic improvement: the curves are smooth with small error bars. The conventional MC results are sometimes even outside the error bar of the PT solution. This is an indication of meta-stable states where the molecule is stuck in a localized region of configuration space. Using a chain of systems with parallel tempering, the meta-stable states are easily sampled at the higher temperatures.

The selectivity at zero loading can be enhanced or impeded by loading effects (molecule–molecule interactions). To examine these effects, we compute the mixture isotherms in the next section. Since we are studying systems under saturation conditions, the framework is fully loaded. The enthalpies of adsorption are large in magnitude. This is partly due to hydrogen bonding but also because of a tight and commensurate fit with the host structure. Dubbeldam et al.[60] conducted a study of hexane isomers in artificial structures, such as carbon sheets, rectangular channels, and cylindrical channels (i.e., carbon nanotubes), where the channel dimensions were systematically varied. At channel dimensions of around 10 Å, the sheet systems show enthalpies in the range of -40 to -50 kJ/mol. Square channels and cylindrical structures bring this down to -70 to -100 kJ/mol because of the overlap of the interaction potentials of the opposing walls. At small channel dimensions of 5–6 Å,

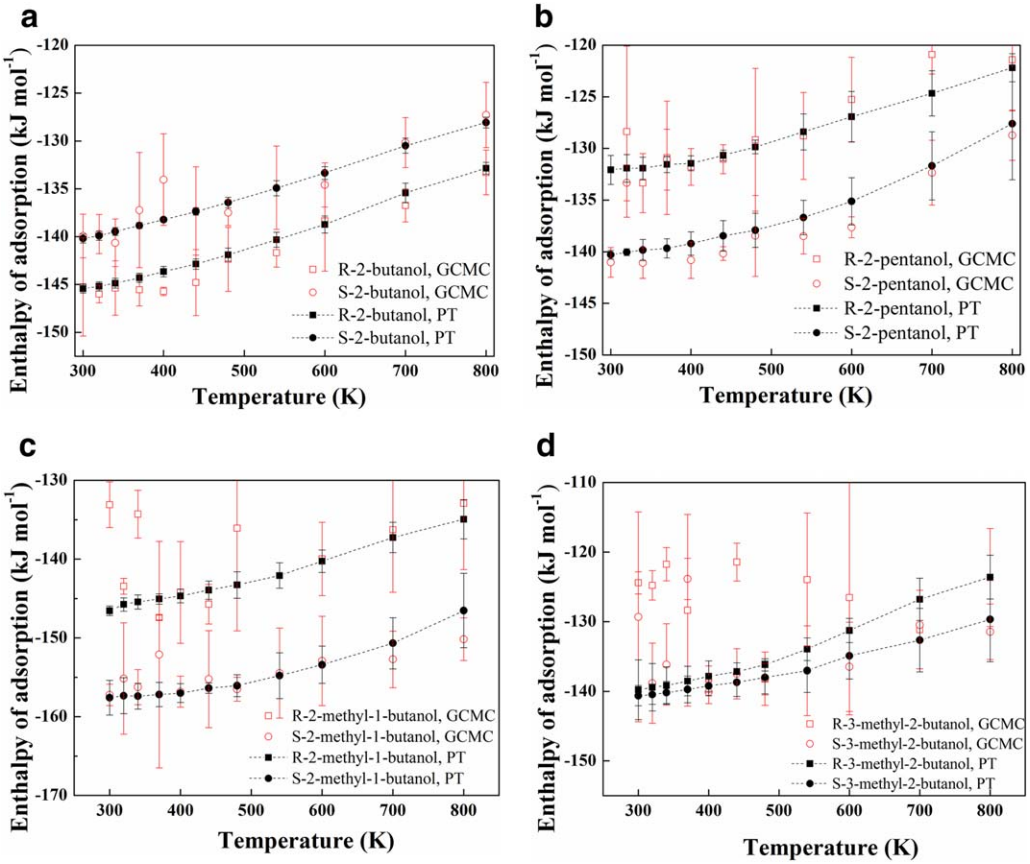

Figure 2. Enthalpies of adsorption at infinite dilution for (a) (R,S)-2-butanol, (b) (R,S)-2-pentanol, (c) (R,S)-2-methyl-1-butanol, and (d) (R,S)-3-methyl-2-butanol using conventional Monte Carlo and parallel tempering.

[Color figure can be viewed in the online issue, which is available at wileyonlinelibrary.com.]

the enthalpies are in the range of −150 to −200 kJ/mol, which indicates an almost ideal match of the shape of the molecule with the shape of the channel. For our system, we have high enthalpies and a strong confinement of the molecules. As shown by the GCMC results below, these systems are hard to sample. It is extremely energetically unfavorable to remove a molecule, while insertion at maximum loading is also close to impossible. An efficient MC mixture move is, therefore, to try to change the identity of a molecule from *R* to *S* or from *S* to *R*, because this energy difference is much smaller than the energy of inserting or deleting a molecule.

(R, S)-2-butanol mixture isotherms

We first performed conventional configurational-bias GCMC simulations of (R,S)-2-butanol adsorption in HOIZA-1 at 300 K in the range of 10^5 to 5×10^6 Pa. The fluid phase composition was held constant at a 50/50 ratio of the *R* and *S* enantiomers. As Figure 3a shows, the loadings of the individual components are noisy and fluctuate around fixed values, but the total loading is constant at the maximum loading of four molec/uc for the fugacities studied here. Under these conditions, the system is semigrand canonical and the property to sample is the ratio of the individual components with a fixed total loading. Note that each point on the isotherm was obtained independently from an initially empty framework. The reason for the large fluctuations is that the number of accepted insertion, deletion, and identity change moves during the simulation under these conditions is virtually zero during the production phase of the simulation. The small number of successful insertion and deletion moves when using conventional GCMC and the resulting inefficient sampling of the phase space lead to poor statistics and a potentially incorrect estimate of the adsorbed phase composition.

Figure 3 also shows the results obtained using PT GCMC and PMF GCMC, which can overcome the problems of conventional GCMC. The total loadings of (R,S)-2-butanol are similar to the values obtained using conventional GCMC, but the loadings of the individual enantiomers are much better sampled and the scatter is substantially reduced.

We calculated the selectivity in the form of the enantiomeric excess (*ee*), which is defined as

$$ee(\%) = \left|\frac{R-S}{R+S}\right| \times 100 \tag{7}$$

where *R* and *S* are the mole fractions of the *R*- and *S*-enantiomers. As shown in Figure 3, the simulations predict an *ee* of ~60% toward R-2-butanol with a roughly constant total loading and selectivity over the fugacity range of $10^5 - 5 \times 10^6$ Pa.

We also studied the siting of the 2-butanol molecules within the pores to better understand the reasons for the observed selectivity. Figure 4 shows a collection of 10 overlaid configurations (i.e., snapshots) of the (R,S)-2-butanol molecules in HOIZA-1 randomly chosen from a simulation at 300 K and 1 bar. There are significant differences between the orientations of the R-2-butanol and the S-2-butanol

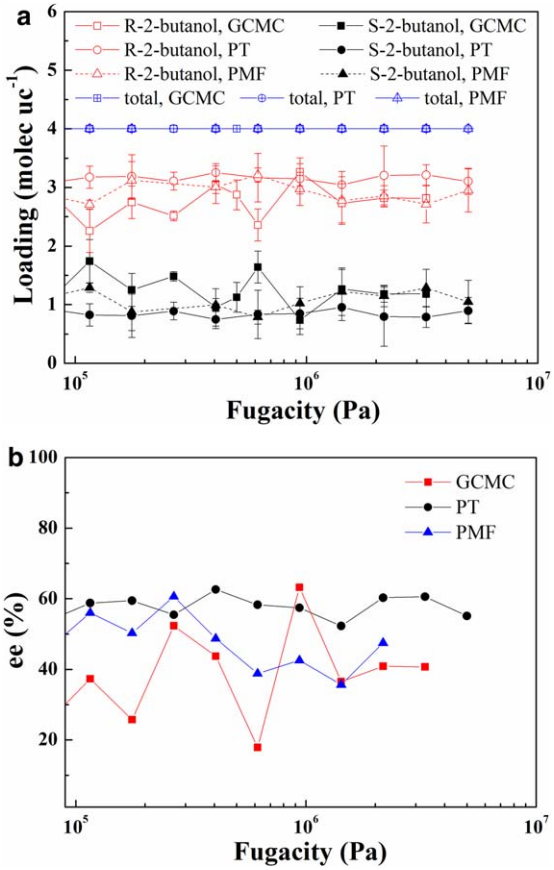

Figure 3. (R,S)-2-butanol in HOIZA-1 at 300 K using conventional GCMC, PT GCMC, and PMF GCMC: (a) isotherms and (b) enantiomeric excess values.

[Color figure can be viewed in the online issue, which is available at wileyonlinelibrary.com.]

molecules inside the pores. In the case of R-2-butanol, most of the —OH groups (shown in red) point toward the pore walls, whereas in the case of S-2-butanol, the —OH groups point toward the inner part of the channels. To quantify the distance of the —OH groups to the pore walls, we calculated the radial distribution function (RDF) between the oxygen atom of the butanol —OH groups and the closest carbon atom of the 2-methoxynaphthalene ligand of the MOF, as shown in Figure 5b.

Figure 5a shows the RDF for both 2-butanol enantiomers. We can see that the —OH group of the R-2-butanol molecule is localized closer to the selected MOF functional group than the —OH group of S-2-butanol, with distances of 4.3 and 5.8 Å, respectively. The different packing of the (R,S)-2-butanol molecules can be seen more clearly in Figure 5b. Even though their alkyl chains are the same, the chirality related to the —OH group makes a great difference. Thus, the different fit of R-2-butanol in the narrow pores compared to S-2-butanol is the reason for the chiral selectivity in HOIZA-1.

Comparison of four chiral alkanols

In addition to (R,S)-2-butanol, we extended our study to include three other chiral alkanols: 2-pentanol, 2-methyl-1-butanol, and 3-methyl-2-butanol. These alkanols are representatives of a family of structurally similar chiral compounds of practical interest.[61,62] Figure 6 shows the adsorption isotherms of these chiral molecules in HOIZA-1, showing that the adsorption preferences for *R* vs. *S* are the same as predicted by the enthalpies of adsorption at infinite dilution. The amount adsorbed follows the order (R,S)-2-butanol > (R,S)-2-methyl-1-butanol ~(R,S)-3-methyl-2-butanol > (R,S)-2-pentanol, reflecting how the different molecule lengths and shapes fit with the pore environment.

Figure 7 shows the enantioselectivities for the different chiral molecules. The highest selectivity is obtained for (R,S)-2-butanol (50–60%) for the *R*-enantiomer, whereas the other molecules exhibit values around 0–20% for the *S*-

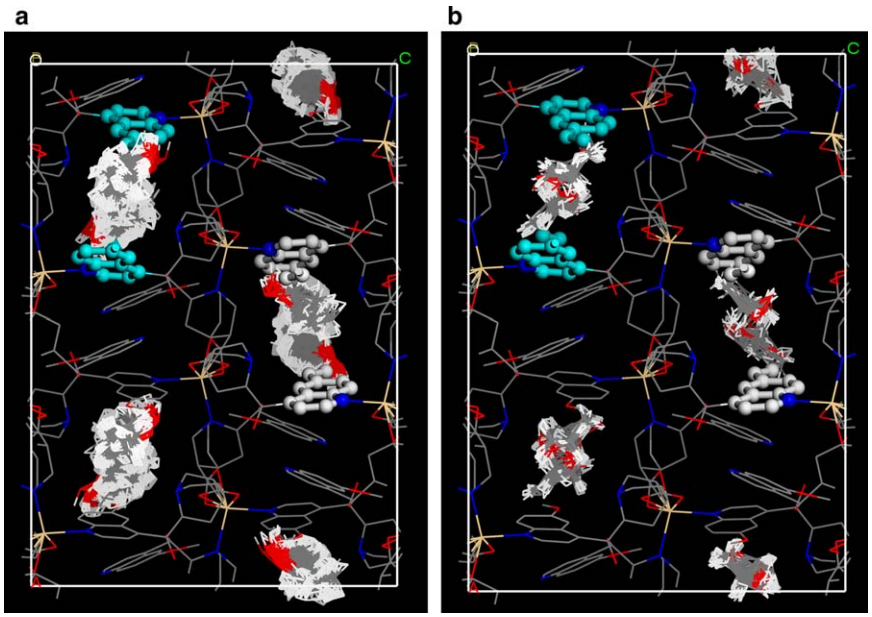

Figure 4. Ten overlapping snapshots of (a) R-2-butanol and (b) S-2-butanol in HOIZA-1 at 300 K and 1 bar.

Red is oxygen, grey is carbon, white is hydrogen, blue is nitrogen, yellow is cadmium, and cyan is the selected functional group for the RDF calculation. [Color figure can be viewed in the online issue, which is available at wileyonlinelibrary.com.]

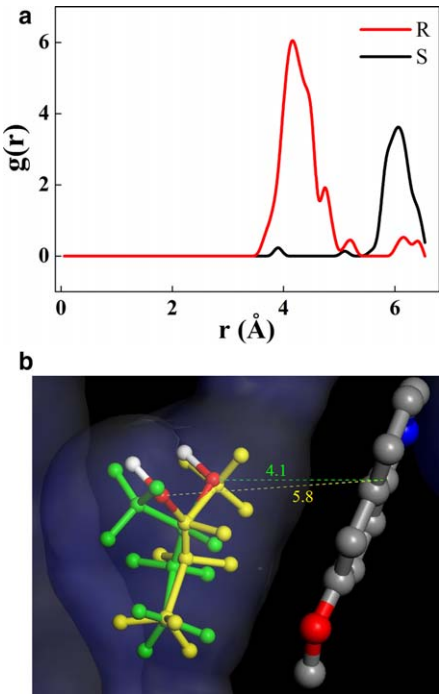

Figure 5. RDFs of (R,S)-2-butanol in HOIZA-1 (a) and representation of (R,S)-2-butanol in the pore and the distances in Å between the butanol —OH and the carbon atom of HOIZA-1 (b).

Green is *R*-molecule; yellow is *S*-molecule; red is oxygen; gray is carbon; blue is nitrogen. [Color figure can be viewed in the online issue, which is available at wileyonlinelibrary.com.]

enantiomer. Xiong et al.[50] mixed HOIZA-1 with racemic mixtures of 2-butanol and 2-methyl-1-butanol and determined by single-crystal X-ray crystallography that the *S* enantiomers were complexed inside the MOF. The *ee* values were estimated as 98 and 8.4% for 2-butanol and 2-methyl-1-butanol, respectively. Our results also predict qualitatively that the *ee* is high for 2-butanol and low for 2-methyl-1-butanol. We predict adsorption of the *S* enantiomer for 2-methyl-1-butanol in agreement with Xiong et al.,[50] but we predict preferential adsorption of R-2-butanol. The reason for this disagreement is not clear.

Figure 8 shows a collection of 10 snapshots of (R,S)-2-butanol, (R,S)-2-pentanol, (R,S)-2-methyl-1-butanol, and (R,S)-3-methyl-2-butanol molecules in HOIZA-1 randomly chosen from simulations at 300 K and 1 bar. The figure shows that the molecules adsorb in discrete sites within the channels and that some molecules fit in these sites better than others. For example, the chain length of (R,S)-2-pentanol is longer than (R,S)-2-butanol, and the pentanol molecules do not fit comfortably in a single site. Therefore, part of the 2-pentanol molecule must enter into one of the connecting sites, leaving empty space in the MOF (indicated by the white circles in Figure 8b). This explains the lower adsorption of 2-pentanol vs. 2-butanol observed in Figure 6. As expected, (R,S)-2-methyl-1-butanol and (R,S)-3-methyl-2-butanol fit very tightly due to their branched chains.

The zero-loading enthalpies of adsorption can be computed very accurately and are a good guideline for what to expect in the mixture isotherms. Any change from the zero-loading trends is due to the effect of loading (adsorbate–adsorbate interactions). For all four molecules, we find the

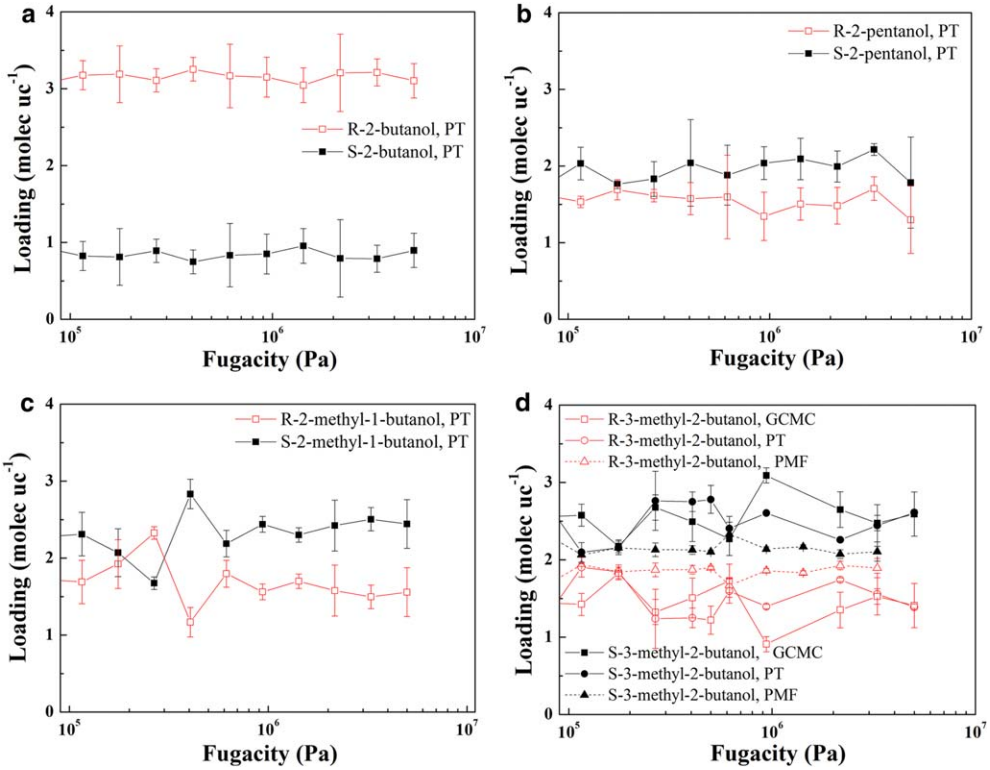

Figure 6. Isotherms for (a) (R,S)-2-butanol, (b) (R,S)-2-pentanol, (c) (R,S)-2-methyl-1-butanol, and (d) (R,S)-3-methyl-2-butanol in HOIZA-1 at 300 K.

[Color figure can be viewed in the online issue, which is available at wileyonlinelibrary.com.]

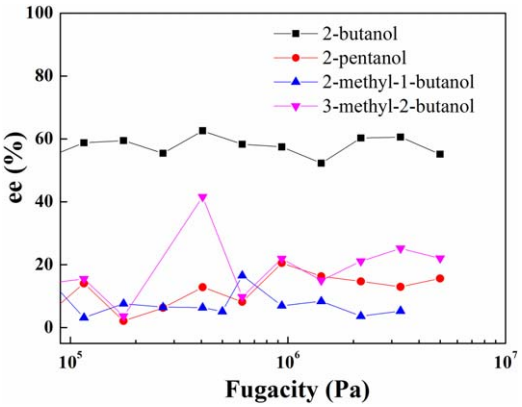

Figure 7. Enantiomeric excess values of four chiral alcohols in HOIZA-1 at 300 K.

[Color figure can be viewed in the online issue, which is available at wileyonlinelibrary.com.]

same ordering in the mixture as from the enthalpies. The snapshots show why: the molecules are localized in discrete framework cavities with limited adsorbate–adsorbate interactions. Thus, the adsorbate–adsorbent interactions dominate the adsorption process. Based on the enthalpies at 300 K, only a small difference (if any) between R-3-methyl-2-butanol and S-3-methyl-2-butanol is expected. The PMF GCMC simulation data (which are the best converged) confirm this expectation.

Comparison of simulation methods

We have demonstrated that at infinite dilution PT shows an order of magnitude improvement over conventional MC. If the PT algorithm is run in parallel on multiple processors, then the results can even be obtained in the same amount of time as conventional MC. Because the replicas on different processors only need to interact during the PT swap moves, the scaling efficiency is close to 100%. The PT methods are

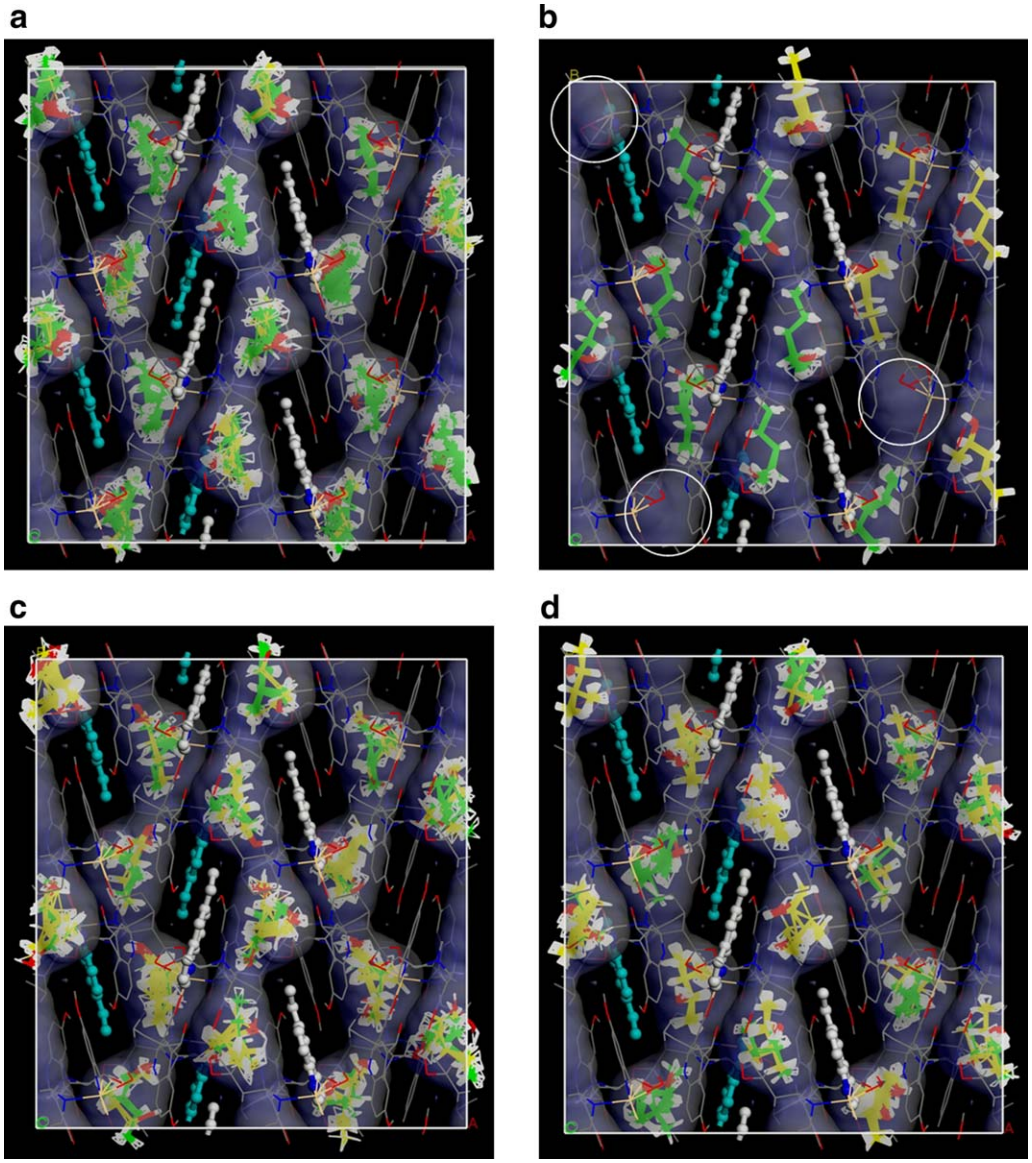

Figure 8. Ten overlapping snapshots of four chiral alcohols in HOIZA-1: (a) (R,S)-2-butanol, (b) (R,S)-2-pentanol, (c) (R,S)-2-methyl-1-butanol, and (d) (R,S)-3-methyl-2-butanol.

Green is *R*-molecule; yellow is *S*-molecule; red is oxygen; gray is carbon; white is hydrogen; blue is nitrogen. [Color figure can be viewed in the online issue, which is available at wileyonlinelibrary.com.]

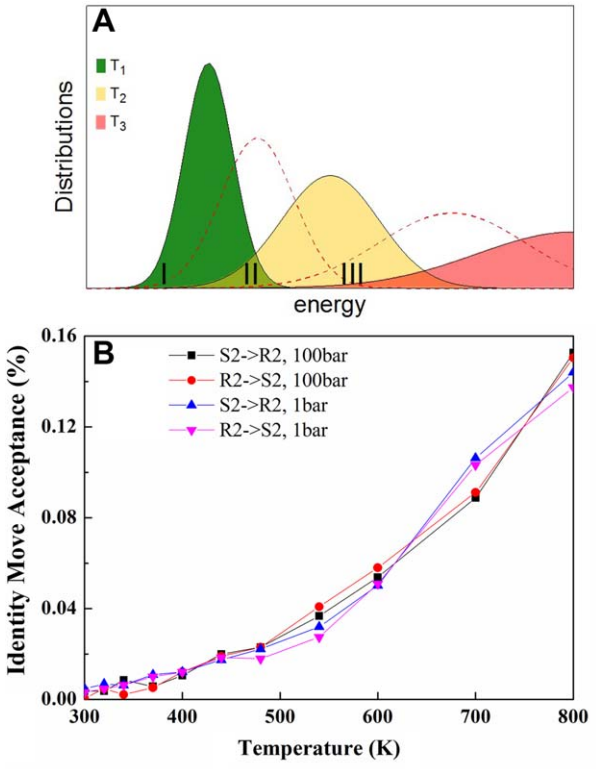

Figure 9. (a) Schematic of PT energy distributions, (b) acceptance ratios of the "identity change" move for (R,S)-2-butanol at 300 K, and 1 and 100 bar.

[Color figure can be viewed in the online issue, which is available at wileyonlinelibrary.com.]

also a powerful way to improve the efficiency and accuracy of GCMC simulations at finite loading. In the liquid-phase systems investigated here, with almost complete saturation of the pores, we found that both PT GCMC and PMF GCMC are superior to conventional GCMC, which had difficulty converging in a reasonable amount of computer time.

In conventional MC, systems can get "stuck" in localized regions of phase space, and getting out of these meta-stable states is a rare event. Using a chain of systems that differ in temperature, parallel tempering reduces, but does not completely eliminate, this problem. Figure 9a shows a schematic of three energy distributions at T_1, T_2, and T_3. The green and yellow distributions overlap (in region II) and in principle acceptance of the PT move should be fine. However, when the system at T_1 is stuck in region I and the neighboring system at T_2 is stuck in region III, then the PT scheme also fails. It is, therefore, advisable to use a rather large number of replicas bridging the system of interest to the higher energy systems. (In Figure 9a, this is denoted by the additional dashed line distributions.) The gain of PT MC as implemented, here, is mainly through an increased acceptance of the "identity change" move (the numbers of successful insertions and deletions are basically zero at saturation conditions). Figure 9b shows the acceptance ratios for the "identity change" move for changing R-2-butanol to S-2-butanol (and vice versa) for 1 bar and 100 bar. The acceptance is too low at 300 K but sufficient at 700 K. Acceptance ratios around 0.1% are low but high enough to provide useful results.[63] In PT, it is essential that the highest chosen temperature system "works." Note that this higher temperature does not have to be "realistic" (the structure is, e.g., not experimentally stable at 700 K) but serves as a computational technique that allows efficient sampling for the lower temperature systems.

The PMF method does not require a calibration of chosen temperatures based on the energy histograms. It uses a chain of systems, ranging from a system fully composed of *R* to a system fully composed of *S* molecules bridged in small steps. By choosing a large number of systems, the energy differences between neighboring systems are small enough to allow a sufficient acceptance rate for swaps. It is, thus, less susceptible to entropic barriers than PT GCMC. The most delicate system here is (R,S)-3-methyl-2-butanol, where at 300 K the two enantiomers have very similar enthalpies of adsorption at infinite dilution. Based on the enthalpies, it is expected that S-3-methyl-2-butanol should be adsorbed more than R-3-methyl-2-butanol, but not by much. Figure 6d shows that PMF GCMC is consistent, while conventional GCMC and PT GCMC give a more scattered picture. Both PT GCMC and PMF GCMC have their merits, and which one to use mainly depends on whether one is interested in a temperature range or a mole fraction range. Both are found to be superior to conventional GCMC.

Conclusions

We used molecular modeling to study the enantioselective adsorption of four alkanols in the HMOF known as HOIZA-1. Conventional GCMC simulations fail due to the low number of accepted insertion and deletion moves. Using PT GCMC and PMF GCMC, we were able to overcome these difficulties. For calculating the enthalpies of adsorption at infinite dilution, PT GCMC displays an order of magnitude improvement over conventional GCMC. PMF GCMC is consistent with PT GCMC, while conventional GCMC gives more scattered loadings. The results show that for R-2-butanol, the —OH groups point toward the pore walls, whereas for S-2-butanol, the —OH groups point toward the middle of the channel. Thus, while their alkyl chains are the same, the chirality related to the —OH group drives selective adsorption of R-2-butanol in HOIZA-1. For four structurally similar chiral alkanols of practical interest, we found that the different molecular sizes and shapes are the main reason for their selective chiral adsorption and that a proper matching of pore size and molecule size is an important design criterion for adsorption and separation in chiral MOFs.

Acknowledgments

Z.W.Q. acknowledges support by the Postgraduate Scholarship Program of the China Scholarship Council (No.2011615050) and the Fundamental Research Funds for the Central Universities (2014ZB0012). D.F.J. thanks the Royal Society (UK) for a University Research Fellowship. D.D. acknowledges support by the Netherlands Research Council for Chemical Science (NWO/CS) through a VIDI grant. R.Q.S. gratefully acknowledges support by the U.S. Department of Energy (DEFG02–08ER15967). J.Z. gratefully acknowledges support by the National Key Basic Research Program of China (No. 2013CB733500) and National Natural Science Foundation of China (Nos. 21376089, 91334202).

Literature Cited

1. Rekoske JE. Chiral separations. *AIChE J*. 2001;47(1):2–5.
2. Ward TJ, Ward KD. Chiral separations: fundamental review 2010. *Anal Chem*. 2010;82:4712–4722.
3. He L, Beesley TE. Applications of enantiomeric gas chromatography: a review. *J Liq Chromatogr Relat Technol*. 2005;28(7):1075–1114.
4. Thompson R. A practical guide to HPLC enantioseparations for pharmaceutical compounds. *J Liq Chromatogr Relat Technol*. 2005; 28(7):1215–1231.
5. Schurig V. Separation of enantiomers by gas chromatography. *J Chromatogr A*. 2001;906(1–2):275–299.
6. Rajendran A, Paredes G, Mazzotti M. Simulated moving bed chromatography for the separation of enantiomers. *J Chromatogr A*. 2009;1216(4):709–738.
7. Lipkowitz KB. Atomistic modeling of enantioselective binding. *Acc Chem Res*. 2000;33(8):555–562.
8. Fitos I, Visy J, Simonyi M, Hermansson J. Separation of enantiomers of benzodiazepines on the Chiral-AGP column. *J Chromatogr A*. 1995;709(2):265–273.
9. Calleri E, Massolini G, Loiodice F, Fracchiolla G, Temporini C, Felix G, Tortorella P, Caccialanza G. Evaluation of a penicillin G acylase-based chiral stationary phase towards a series of 2-aryloxyalkanoic acids, isosteric analogs and 2-arylpropionic acids. *J Chromatogr A*. 2002;958(1–2):131–140.
10. Roussel C, Suteu C, Shaimi L, Soufiaoui M. Structure and substituent effect on chiral separation of some 4a-methyl-2, 3, 4, 4a-tetrahydro-1H-fluorene derivatives and 4a-methyl-1, 2, 3, 4, 4a, 9a-hexahydro-fluoren-9-one derivatives on CTA-I and chiralcel OJ chiral stationary phases. *Chirality*. 1998;10(6):522–527.
11. Jin YZ, Hirose K, Nakamura T, Nishioka R, Ueshige T, Tobe Y. Preparation and evaluation of a chiral stationary phase covalently bound with a chiral pseudo-18-crown-6 ether having a phenolic hydroxy group for enantiomer separation of amino compounds. *J Chromatogr A*. 2006;1129(2):201–207.
12. Tanaka D, Kitagawa S. Template effects in porous coordination polymers. *Chem Mater*. 2007;20(3):922–931.
13. Snurr RQ, Hupp JT, Nguyen ST. Prospects for nanoporous metal-organic materials in advanced separations processes. *AIChE J*. 2004; 50(6):1090–1095.
14. Rowsell JLC, Yaghi OM. Metal-organic frameworks: a new class of porous materials. *Microporous Mesoporous Mater*. 2004;73(1):3–14.
15. Maspoch D, Ruiz-Molina D, Veciana J. Old materials with new tricks: multifunctional open-framework materials. *Chem Soc Rev*. 2007;36(5):770–818.
16. Lin W. Metal-organic frameworks for asymmetric catalysis and chiral separations. *MRS Bull*. 2007;32(07):544–548.
17. Lee S, Mallik AB, Xu Z, Lobkovsky EB, Tran L. Small amphiphilic organics, coordination extended solids, and constant curvature structures. *Acc Chem Res*. 2005;38(4):251–261.
18. Kitagawa S, Kitaura R, Noro S. Functional porous coordination polymers. *Angew Chem Int Ed*. 2004;43(18):2334–2375.
19. Kesanli B, Lin W. Chiral porous coordination networks: rational design and applications in enantioselective processes. *Coord Chem Rev*. 2003;246(1–2):305–326.
20. Férey G. Hybrid porous solids: past, present, future. *Chem Soc Rev*. 2007;37(1):191–214.
21. Eddaoudi M, Moler DB, Li H, et al. Modular chemistry: secondary building units as a basis for the design of highly porous and robust metal-organic carboxylate frameworks. *Acc Chem Res*. 2001;34(4):319–330.
22. Bradshaw D, Claridge JB, Cussen EJ, Prior TJ, Rosseinsky MJ. Design, chirality, and flexibility in nanoporous molecule-based materials. *Acc Chem Res*. 2005;38(4):273–282.
23. Seo JS, Whang D, Lee H, Im Jun S, Oh J, Jeon YJ, Kim K. A homochiral metal-organic porous material for enantioselective separation and catalysis. *Nature*. 2000;404(6781):982–986.
24. Bradshaw D, Prior TJ, Cussen EJ, Claridge JB, Rosseinsky MJ. Permanent microporosity and enantioselective sorption in a chiral open framework. *J Am Chem Soc*. 2004;126(19):6106–6114.
25. Dybtsev DN, Nuzhdin AL, Chun H, Bryliakov KP, Talsi EP, Fedin VP, Kim K. A homochiral metal-organic material with permanent porosity, enantioselective sorption properties, and catalytic activity. *Angew Chem Int Ed*. 2006;45(6):916–920.
26. Bao XY, Broadbelt LJ, Snurr RQ. Computational screening of homochiral metal-organic frameworks for enantioselective adsorption. *Microporous Mesoporous Mater*. 2012;157:118–123.
27. Qiao Z, Zhou J, Lu X. Designing new amine functionalized metal-organic frameworks for carbon dioxide/methane separation. *Fluid Phase Equilib*. 2014;362:342–348.
28. Macedonia MD, Maginn EJ. A biased grand canonical Monte Carlo method for simulating adsorption using all-atom and branched united atom models. *Mol Phys*. 1999;96(9):1375–1390.
29. Qiao Z, Ren S, Zhou J. Molecular simulations of adsorption and separation of H2S and N2 mixture by single wall carbon nanotubes. *Chem J Chin Univ*. 2012;33(4):800–805.
30. Smit B, Krishna R. Monte Carlo simulations in zeolites. *Curr Opin Solid State Mater Sci*. 2001;5(5):455–462.
31. Qiao Z, Wu Y, Li X, Zhou J. Molecular simulation on the separation of water/ethanol azeotropic mixture by poly (vinyl alcohol) membrane. *Fluid Phase Equilib*. 2011;302(1):14–20.
32. Moghadam PZ, Duren T. Origin of Enantioselectivity in a chiral metal-organic framework: a molecular simulation study. *J Phys Chem C*. 2012;116(38):20874–20881.
33. Nita S, Cann NM. Solvation of phenylglycine- and leucine-derived chiral stationary phases: molecular dynamics simulation study. *J Phys Chem B*. 2008;112(41):13022–13037.
34. Ashtari M, Cann NM. Poly-proline-based chiral stationary phases: a molecular dynamics study of triproline, tetraproline, pentaproline, and hexaproline interfaces. *J Chromatogr A*. 2012;1265:70–87.
35. Pecheanu R, Cann NM. Molecular dynamics simulations of the liquid-crystal phases of 2-(4-butyloxyphenyl)-5-octyloxypyrimidine and 5-(4-butyloxyphenyl)-2-octyloxypyrimidine. *Phys Rev E*. 2010; 81(4):041704.
36. Bao XY, Broadbelt LJ, Snurr RQ. A computational study of enantioselective adsorption in a homochiral metal-organic framework. *Mol Simul*. 2009;35(1–2):50–59.
37. Bao XY, Snurr RQ, Broadbelt LJ. Collective effects of multiple chiral selectors on enantioselective adsorption. *Langmuir*. 2009;25(18): 10730–10736.
38. Bao XY, Broadbelt LJ, Snurr RQ. Elucidation of consistent enantioselectivity for a homologous series of chiral compounds in homochiral metal-organic frameworks. *Phys Chem Chem Phys*. 2010;12(24): 6466–6473.
39. Siepmann JI, Frenkel D. Configurational bias Monte Carlo: a new sampling scheme for flexible chains. *Mol Phys*. 1992;75(1):59–70.
40. Vlugt TJH, Krishna R, Smit B. Molecular simulations of adsorption isotherms for linear and branched alkanes and their mixtures in silicalite. *J Phys Chem B*. 1999;103(7):1102–1118.
41. Geyer CJ, Thompson EA. Annealing Markov chain Monte Carlo with applications to ancestral inference. *J Am Stat Assoc*. 1995:90; 909–920.
42. Hansmann UHE. Parallel tempering algorithm for conformational studies of biological molecules. *Chem Phys Lett*. 1997;281(1–3): 140–150.
43. Tesi MC, Rensburg EJJ, Orlandini E, Whittington SG. Monte Carlo study of the interacting self-avoiding walk model in three dimensions. *J Stat Phys*. 1996;82(1):155–181.
44. Earl DJ, Deem MW. Parallel tempering: theory, applications, and new perspectives. *Phys Chem Chem Phys*. 2005;7(23):3910–3916.
45. Xie Y, Zhou J, Jiang S. Parallel tempering Monte Carlo simulations of lysozyme orientation on charged surfaces. *J Chem Phys*. 2010; 132:065101.
46. Punnathanam S, Denayer JFM, Daems I, Baron GV, Snurr RQ. Parallel tempering simulations of liquid-phase adsorption of n-alkane mixtures in zeolite LTA-5A. *J Phys Chem C*. 2011;115:762–769.
47. van Erp TS, Dubbeldam D, Caremans TP, Calero S, Martens JA. Effective Monte Carlo scheme for multicomponent gas adsorption and enantioselectivity in nanoporous materials. *J Phys Chem Lett*. 2010;1(14):2154–2158.
48. Caremans TP, van Erp TS, Dubbeldam D, Castillo JM, Martens JA, Calero S. Enantioselective adsorption characteristics of aluminum-substituted MFI zeolites. *Chem Mater*. 2010;22(16):4591–4601.
49. Beerdsen E, Dubbeldam D, Smit B. Loading dependence of the diffusion coefficient of methane in nanoporous materials. *J Phys Chem B*. 2006;110(45):22754–22772.
50. Xiong RG, You XZ, Abrahams BF, Xue Z, Che CM. Enantioseparation of racemic organic molecules by a zeolite analogue. *Angew Chem Int Ed*. 2001;40(23):4422–4425.
51. Gelb LD, Gubbins KE. Pore size distributions in porous glasses: a computer simulation study. *Langmuir*. 1999;15(2):305–308.
52. Rappe AK, Casewit CJ, Colwell KS, Goddard III WA, Skiff WM. UFF, a full periodic table force field for molecular mechanics and

molecular dynamics simulations. *J Am Chem Soc*. 1992;114(25): 10024–10035.
53. Jorgensen WL. Optimized intermolecular potential functions for liquid alcohols. *J Phys Chem*. 1986;90(7):1276–1284.
54. Jorgensen WL, Maxwell DS, Tirado-Rives J. Development and testing of the OPLS all-atom force field on conformational energetics and properties of organic liquids. *J Am Chem Soc*. 1996;118(45): 11225–11236.
55. Breneman CM, Wiberg KB. Determining atom-centered monopoles from molecular electrostatic potentials. The need for high sampling density in formamide conformational analysis. *J Comput Chem*. 1990;11(3):361–373.
56. Lee C, Yang W, Parr RG. Development of the Colle-Salvetti correlation-energy formula into a functional of the electron density. *Phys Rev B*. 1988;37(2):785–789.
57. Becke AD. Density-functional thermochemistry. III. The role of exact exchange. *J Chem Phys*. 1993;98:5648–5652.
58. Ewald PP. The calculation of optical and electrostatic grid potential. *Ann Phys (N Y)*. 1921;64(3):253–287.
59. Geyer CJ, Thompson EA. Annealing Markov chain Monte Carlo with applications to ancestral inference. *J Am Stat Assoc*. 1995;90: 909–920.
60. Dubbeldam D, Krishna R, Calero S, Yazaydın AÖ. Computer-assisted screening of ordered crystalline nanoporous adsorbents for separation of alkane isomers. *Angew Chem Int Ed*. 2012;124(47): 12037–12041.
61. Kim CU, Lew W, Williams MA, Wu H, Zhang L, Chen X, Escarpe PA, Mendel DB, Laver WG, Stevens RC. Structure-activity relationship studies of novel carbocyclic influenza neuraminidase inhibitors. *J Med Chem*. 1998;41(14):2451–2460.
62. Ebner DC, Trend RM, Genet C, McGrath MJ, O'Brien P, Stoltz BM. Palladium-catalyzed enantioselective oxidation of chiral secondary alcohols: access to both enantiomeric series. *Angew Chem Int Ed*. 2008;47(34):6367–6370.
63. Mezei M. A cavity-biased (T, V, μ) Monte Carlo method for the computer simulation of fluids. *Mol Phys*. 1980;40(4):901–906.

Manuscript received Sept. 7, 2013, revision received Dec. 20, 2013, and final revision received Feb. 12, 2014.